Preequilibrium (p,n) reaction as a probe for the effective nucleon-nucleon interaction in multistep direct processes

W. Scobel and M. Trabandt
I. Instituut für Experimentalphysik, Universität Hamburg, D-2000 Hamburg 50, Federal Republic of Germany

M. Blann, B. A. Pohl, and B. R. Remington
Lawrence Livermore National Laboratory, Livermore, California 94550

R. C. Byrd
Los Alamos National Laboratory, Los Alamos, New Mexico 87545

C. C. Foster
Indiana University Cyclotron Facility, Indiana University, Bloomington, Indiana 47405

R. Bonetti and C. Chiesa
Istituto de Fisica Generale Applicata, dell'Università di Milano, Italy

S. M. Grimes
Ohio University, Athens, Ohio 45701
(Received 13 November 1989)

The spectral continua $E_n \geq 30$ MeV of neutrons from the reactions ^{27}Al, ^{90}Zr, ^{208}Pb(p,xn) have been measured for $E_p = 120$ and 160 MeV and angles $0° \leq \theta \leq 145°$. Angular distributions can be explained quantitatively in absolute values and shapes over five orders of magnitude as statistical multistep direct emission in which up to six steps are involved with significant contributions. The strength V_0 of the effective nucleon-nucleon interaction applied shows a systematic dependence on the projectile energy $E_p \leq 160$ MeV that is consistent with that of spectroscopic factors for single step distorted-wave Born approximation results for transitions to low-lying states. The data also agree well with predictions of a recent phenomenological parametrization.

I. INTRODUCTION

The statistical multistep model of Feshbach, Kerman, and Koonin[1] (FKK) is directed at a formal and conceptual unification of various reaction mechanisms ranging from single-step direct reactions via preequilibrium (PE) processes to the compound nucleus formation. It is mediated by the incoherent contributions of the statistical multistep compound (SMCE) and direct emission (SMDE), where the SMDE process dominates the continuum region of the nucleon energy spectra more, the higher the projectile energy.

This model has been successfully applied to (p,n) reactions for projectile energies up to 45 MeV,[2,3] and it was found that three or fewer nucleon-nucleon scattering steps were sufficient to reproduce the major fraction of the PE cross section as anticipated from Ref. 4. The effective nucleon-nucleon (NN) interaction for the calculation of the distorted-wave Born approximation (DWBA) form factor herein could be given a Yukawa shape of range $r_0 = 1.0$ fm and strength $V_0 = 26 \pm 1$ MeV in full consistency with SMCE and single-step DWBA calculations.[5,6] Recently, evidence was reported[7] for the necessity to reduce V_0 to 20 ± 1 MeV in SMDE calculations for (p,n) reactions with 80 MeV projectiles.

It is known[8,9] that the central scalar-isoscalar part of the effective NN interaction decreases with increasing bombarding energy. If the (p,n) PE process probes this interaction and is adequately described as an SMDE mechanism, a further decrease of V_0 with increasing E_p, as well as an enhanced importance of higher step contributions due to the extended equilibration phase, should be anticipated. In the present work we test the SMDE approach in this respect for the first time with projectile energies $E_p > 100$ MeV.

In addition, we shall compare the relative contributions of higher order steps for the SMDE model with those obtained for a semiclassical PE model and relate existing discrepancies to the disagreement the latter model exhibits in comparison with experimental angular distributions in the backward hemisphere.

In Sec. II we describe our experimental setup. Section III is devoted to a qualitative discussion of the experimental results as well as the comparison with a phenomenological parametrization of PE angular distributions. In Sec. IV we analyze our data with the FKK multistep model, with a summary given in Sec. V.

II. EXPERIMENTAL TECHNIQUE

The general experimental setup has been discussed in detail elsewhere.[7] Here we give only a short description

with emphasis on modifications introduced for the study presented.

The experiment was performed with the neutron time-of-flight (TOF) set up of the Indiana University Cyclotron Facility (IUCF).[10] The 120 and 160.3 MeV proton beams were given a burst width ≤ 700 ps and a separation of 1.8 μs by means of the stripper loop.[11] The resulting beam had an average intensity of 40–80 nA at the beam swinger; it was focused onto self-supporting targets of isotopically enriched (^{90}Zr: 97.6%; ^{208}Pb: 98.7% and 99.9%) material of different thicknesses (^{27}Al: 180 mg/cm^2; ^{90}Zr: 77 and 112 mg/cm^2; ^{208}Pb: 102 and 176 mg/cm^2). The beam swinger[10] was operated with deflection angles of 0°, 11°, and 24°, respectively. We used five fixed detectors covering the angular range from 0° to 145° with the TOF path lengths given in Table I.

The neutron detectors consisted of cylindrical cells (30.5 cm in diam. $\times$ 20.3 cm) filled with the liquid scintillator BC 501; they were supplemented by sheets of plastic scintillator placed in front of and on top of the cells for discrimination against protons and for suppression of cosmic radiation. The detectors were operated with n-γ pulse-shape discrimination. For neutron background determination, each run was accompanied by a background run with shadow bars of appropriate length that were placed approximately midway between targets and detectors and resulted in an absorption $\geq 96\%$ for $E_n \leq 160$ MeV. For each event the neutron TOF, pulse height, pulse shape, and identification signal were registered. The hardware thresholds were set to values $E_{\rm th}^n \approx 14$ MeV that gave overall and long term time resolutions $\Delta t_n \leq 2.5$ ns (including a beam contribution of less than 700 ps). The corresponding worst case energy resolutions are given in Table I for $E_n = 100$ MeV.

The neutron TOF spectra were converted into energy spectra and transformed into double differential cross sections in the center-of-mass (c.m.) system with the efficiencies $\eta(E_n, E_{\rm th}^s)$ taken from Ref. 12 for software thresholds $E_{\rm th}^s = 20$ MeV including some consistency checks for higher threshold values [Fig. 1(a)]. In addition, η was determined experimentally from the ^{7}Li(p,n_{0+1}) reaction at $\theta_{\rm lab} = 0°$ with the cross sections reported in Ref. 13. It was found that the experimental values for η deviate up to 14% from the calculated[12] ones.

On their flight paths, the neutrons traverse some construction material and air, as well as aluminum and copper plates that were inserted to suppress elastically scattered protons. The maximum thicknesses for the relevant materials are given in Table I. The flux attenuation reaches values of $\leq 30\%$ for $E_n \geq 50$ MeV and corrections were made for this. Test runs with additional material in the TOF paths showed [Fig. 1(b)] that the correction is, in most cases, accurate to within 3%. The relative uncertainties within angular distributions are mostly due to target inhomogeneities (5%), inconsistencies in the background treatment (10%), and incomplete beam-current integration (4%). The estimated error margin is 14%. Absolute uncertainties include those of the detector efficiencies[14] and are slightly higher ($\leq 20\%$). The count rate loss encountered with detector 4 for angles 88°–106° in the preceding experiment[7] could be reduced, in particular, for $E_p = 160$ MeV, but not totally avoided in the present experiment (cf. Figs. 5 and 6), because the target collimator geometry allowed only for a restricted realignment.

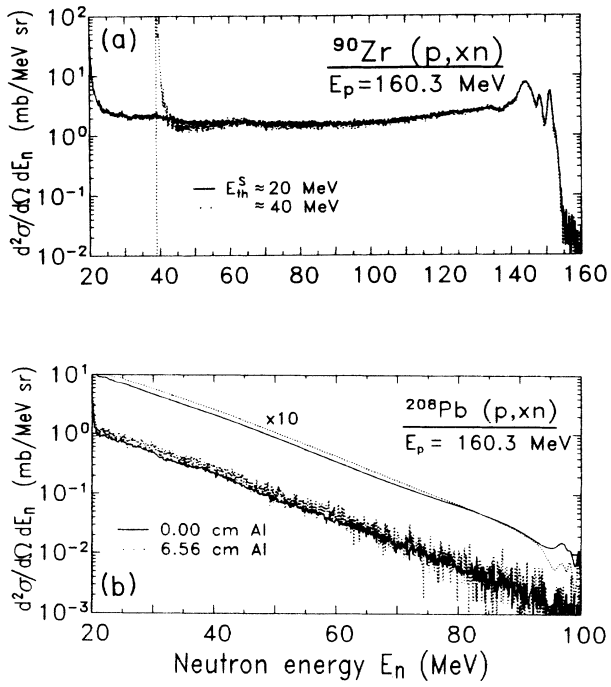

FIG. 1. (a) Energy spectrum obtained under $\theta_{\rm lab} = 0°$ from evaluation with a software threshold $E_{\rm th}^s$ of 20 and 40 MeV. (b) Effect of additional absorber material (6.56 cm Al) on the measurement for $\theta_{\rm lab} = 145°$ with 160 MeV protons. The spectra after smoothing and multiplication by a factor 10 are shown as well.

TABLE I. Neutron detector data; ΔE_n is given for a time resolution $\Delta t = 2.5$ ns and includes a target thickness $\Delta E_p = 400$ keV.

Detector number	$\theta_{\rm lab}$ (deg)	TOF (m)	$d_{\rm Al}$ (mm)	$d_{\rm Cu}$ (mm)	ΔE_n (MeV)
1	0°, 11°, 24°	60.7	0.75	≤ 19	1.2
2	24°, 35°, 48°	47.6	0.75	≤ 25	1.5
3	45°, 56°, 69°	34.8	4.80	≤ 25	2.0
4	106°, 95°, 82°	12.0	2.75	≤ 19	5.8
5	145°, 134°, 121°	12.6	34.5		5.5

III. EXPERIMENTAL RESULTS

A. General features

A representative selection of neutron energy spectra from the reaction of 120 and 160 MeV protons with ^{27}Al, ^{90}Zr, and ^{208}Pb is shown in Figs. 2–4. The isobaric analog state (IAS) visible in the 0° spectra for ^{90}Zr as well as the Gamov-Teller [(GT); $L=0$)] resonance and the spin-flip dipole ($L=1$) and quadrupole ($L=2$) mode are in quantitative agreement with published results in energies and widths.[15,16] Integration of the peaks (for $E_p=120$ MeV) yields 7,0±0.7 (22.2±0.9; 9.0±0.9) mb/sr for the IAS (GT; $L=1$). The corresponding[15] numbers are 6.0±0.7 (23±2.8; 7.9±1.6) mb/sr; they confirm the absolute cross sections of the present work. Moreover, results for $\theta=24°$ were obtained with two adjacent detectors during different beam swinger settings; they agreed to within a few percent and strengthened the consistency of the individual spectra and thus the angular distributions derived. For the reaction ^{208}Pb(p,n), the IAS is on top of the GT resonance and gives rise to a broad structure (cf. Fig. 4). The collective strength visible in Figs. 2 and 3 for the angles $\theta_{lab}=0°$ and 11° cannot be accounted for with a model description based on nucleon-nucleon collisions. This point will be discussed in Sec. IV.

In the continuum region displayed in Figs. 2–4, the spectra undergo a characteristic transition from a very weak neutron energy dependence under very forward angles to an almost exponential shape for the most backward angles. Their slopes, however, are incompatible

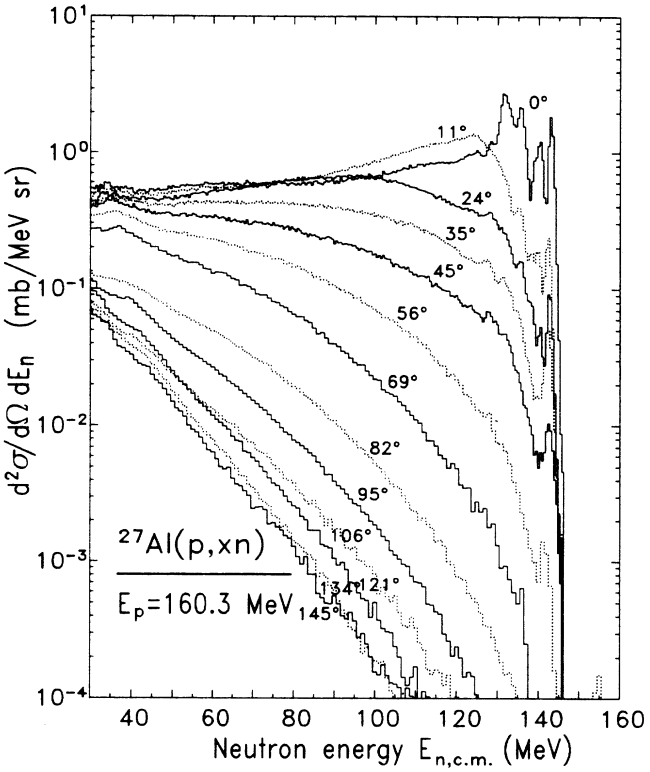

FIG. 2. Experimental energy spectra for the reaction ^{27}Al(p,n) and selected angles. This reaction was not measured for $E_p=120$ MeV. The (p,n) Q value is −5.59 MeV.

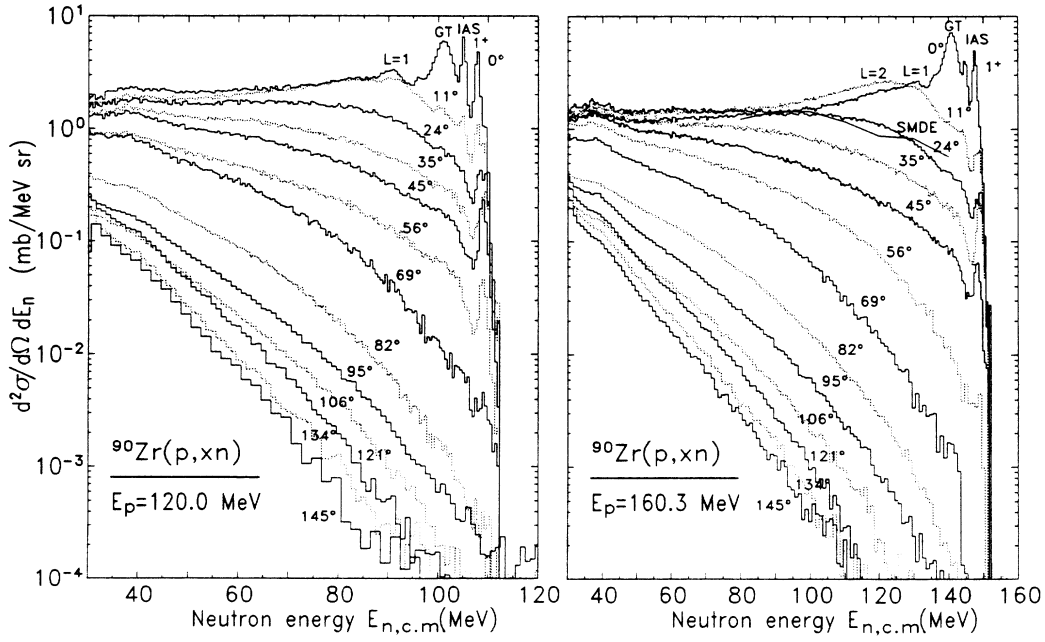

FIG. 3. Same as in Fig. 2 for ^{90}Zr(p,n). Also shown (for $E_p=160$ MeV) is the normalized SMDE calculation for $\theta_{lab}=20°$; $Q_{pn}=-6.89$ MeV.

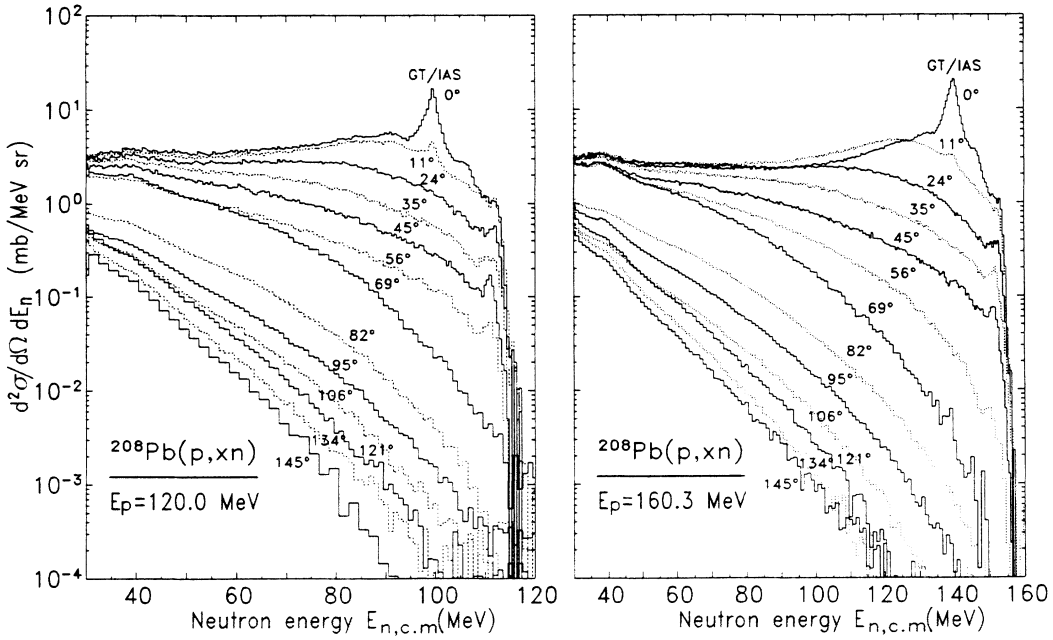

FIG. 4. Same as in Fig. 2 for ^{208}Pb(p,n); $Q_{pn} = -3.66$ MeV.

with those of an equilibrated system. The reaction $p+^{90}\mathrm{Zr} \rightarrow ^{91}\mathrm{Nb}^*$ leads to the initial excitation energies, of the composite nucleus (CN) E^*_{CN}, given in Table II for the three projectile energies of this work and Ref. 7. The anticipated slope parameters $T_{\mathrm{CN}} = (E^*_{\mathrm{CN}}/a)^{1/2}$ are calculated with a level density parameter $a = A/8.5$ MeV^{-1}; they are about a factor of 3 smaller than the values $T(\theta = 145°)$ which can be read from the most backward spectra. In addition, the experimental slopes $T(\theta = 145°)$ do not vary with target mass number A, but are the same for $p+^{27}\mathrm{Al},^{90}\mathrm{Zr},^{208}\mathrm{Pb}$ within the uncertainties stated in Table II. Moreover, the angular distributions do not show a tendency to increase again beyond 90° even for the lowest neutron energies $E_n = 30$–40 MeV.

Therefore, sizeable contributions from a statistically equilibrated system or a process that is adequately described as a statistical multistep compound emission (SMCE) can certainly be excluded for $E_n \geq 40$ MeV. Rather, the data presented—with the exception of the region of collective resonances under very forward angles—carry information on nucleon-nucleon collisions in bulk nuclear material, i.e., the effective nucleon-nucleon interaction. If so, the data should not depend on the detailed nuclear structure of the target, but follow a general and smooth trend with target mass number and ejectile energy that is accessible to extrapolations.

TABLE II. Excitation E^*_{CN} and temperature T_{CN} of the compound nucleus ^{91}Nb* and the experimental slope values T $(\theta = 145°)$. All energies are given in MeV.

E_p	80.5	120	160.3
E^*_{CN}	84.9	124.0	163.8
T_{CN}	2.8	3.4	3.9
T $(\theta = 145°)$	7.9±0.3	8.0±0.3	11.4±0.3

B. Preequilibrium parametrizations and models

Kalbach has recently shown[17] that angular and spectral shapes of inclusive double differential cross sections for transitions populating the spectral continuum can be parametrized in a phenomenological way as

$$\frac{d^2\sigma}{d\Omega\, d\epsilon} = a_0^{\mathrm{MSD}} \exp(a\cos\theta) + a_0^{\mathrm{MSC}}[\exp(a\cos\theta) + \exp(-a\cos\theta)] \,. \quad (1)$$

Here, a_0^{MSD} fixes the absolute cross section of the forward peaked contribution from the multistep direct emission, and a_0^{MSC} the multistep compound contribution which, by construction of Eq. (1), is symmetric around 90°. The values for a_0^{MSD} and a_0^{MSC} can be taken from a semiclassical PE model or a normalization. The dependence of the slope parameter $a(E_{\mathrm{proj}}, \epsilon)$ on projectile kind and energy E_{proj}, and on the ejectile energy ϵ was derived from a large body of data for light projectiles with energies up to 600 MeV. The slope parameter a is predicted to depend (i) strongly on ϵ, (ii) for a given ϵ also on E_{proj}, and (iii) practically not on the target nuclide. Here, Eq. (1) will be applied under the assumption of 100% MSD contribution with a_0^{MSD} being chosen to reproduce the angle integrated neutron energy spectra.

In Fig. 5(a), our ^{208}Pb(p,xn) angular distributions for $E_p = 160$ MeV are compared to this parametrization. The dependence on E_n is very pronounced. Whereas, for $E_n = 40$ MeV a reduction of the cross sections from very forward to backward angles by a factor of 10 is observed, the experimental distribution spans more than 5 orders of magnitude at $E_n = 140$ MeV. The normalized results of Eq. (1) follow this shape transition reasonably well. The same extent of agreement is found for ^{90}Zr(p,xn), cf. Fig.

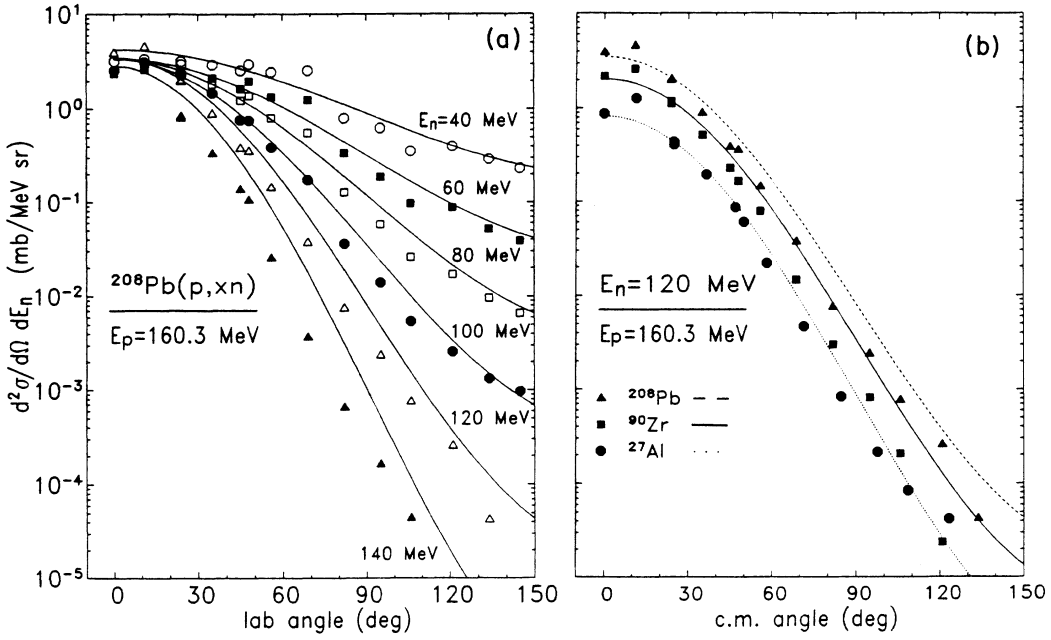

FIG. 5. Experimental angular distributions compared to the results (lines) of Eq. (1) for (a) ^{208}Pb(p,n) at $E_p = 160$ MeV and several c.m. ejectile energies; (b) for $E_p = 160$ MeV and $E_{n,\mathrm{c.m.}} = 120$ MeV from all three targets under study.

7. As stated before, the systematics suggest that the angular distributions at high neutron energies will show no shape dependence on the target. The comparison of the data for $p+^{27}$Al, ^{90}Zr, and ^{208}Pb in Fig. 5(b) does in fact show the same shape over several orders of magnitude down to the 10^{-1}–10^{-2} μb/sr MeV level where they are limited by statistical and background inaccuracies. The description of these data with Eq. (1) reproduces this mass independent shape. The deviations at $\theta = 11°$ originate from the contribution of the $L = 2$ quadrupole resonance.

Figure 6 demonstrates that our data in combination with those[7] for $E_p = 80$ MeV exhibit a dependence of the shapes on E_p. Therefore, they rule out the older[18] parametrization intended for lower projectile and ejectile energies, whereas Eq. (1) works well. For the higher projectile energy $E_p = 160$ MeV and a given neutron energy, the angular distributions turn flatter and thus may indicate the importance of higher order steps with increasing inelasticity.

It has been repeatedly[7,19,20] reported for nucleon projectile energies up to 90 MeV that semiclassical preequilibrium models based on an intranuclear nucleon-nucleon-collision process fail to reproduce angular distributions. This applies even more at higher projectile energies. As an example we show in Fig. 7 the prediction of the geometry dependent hybrid (GDH) model[21] with the assumption of a pure intranuclear nucleon-nucleon scattering mechanism without any *ad hoc* modifications.[19] It must be pointed out, however, that this failure, although of principal nature, does not devaluate these models for application to angle integrated energy spectra and related applications as will be shown shortly.

In the GDH model, the energy differential cross section for nucleon ejectiles ν of energy ϵ is

$$\frac{d\sigma_\nu}{d\epsilon} = \pi\lambda^2 \sum_l (2l+1) T_l(\epsilon) P_{l\nu}(\epsilon) \ , \tag{2}$$

with a sum that extends over partial-wave contributions, each of which is proportional to the product of the

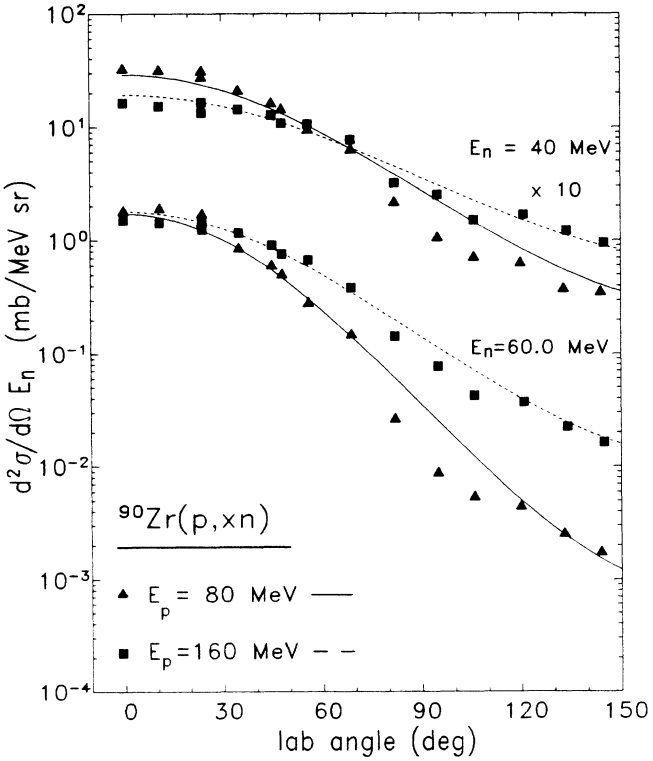

FIG. 6. Experimental angular distributions of 40 and 60 MeV neutrons (c.m.) from $p+^{90}$Zr with different projectile energies. The lines are the normalized results of Eq. (1).

transmission coefficient $T_l(\epsilon)$ and the emission probability $P_{l\nu}(\epsilon)$. The latter is calculated from Pauli-corrected partial-state densities, an emission rate into the continuum based on the principle of detailed balance, and from intranuclear transition rates, $\lambda_+^{NN}(\epsilon)$, leading via nucleon-nucleon collisions to states of increasing complexity. The Fermi energy and transition rates $\lambda_+^{NN}(\epsilon)$ are the density-weighted average over the entrance channel trajectory for each partial wave l, whereas in the standard hybrid model the average is taken over the whole target nucleus such that Eq. (2) reduces to one term, namely $\sigma_R P_\nu(\epsilon)$. All calculations presented here were performed with the default parameter values.[21] In Fig. 8, the results are compared with the angle integrated experimental spectra for the system $p+^{90}$Zr. We find an overall agreement in absolute cross section to within 30% without any parameter adjustment. In the high energy parts of the spectra, the calculation tends to overestimate the experiment; this effect is less pronounced for the standard hybrid model than for the GDH model. The same observation was made for $E_p = 80$ MeV.[7] It indicates that

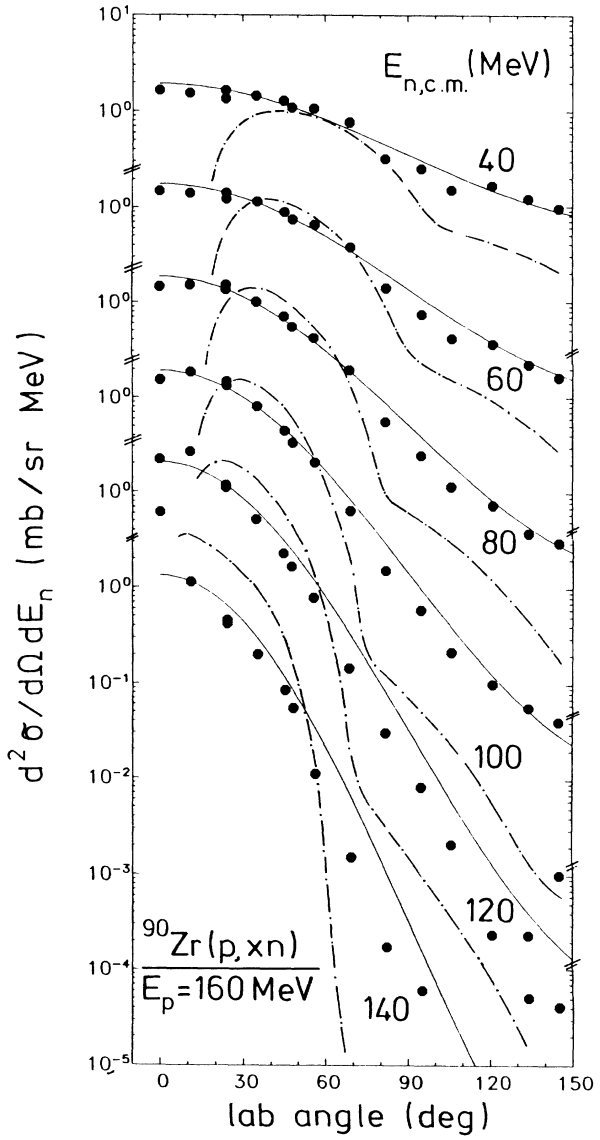

FIG. 7. Experimental angular distributions in comparison to the normalized results of Eq. (1) (solid line) and the GDH model prediction (dashed line).

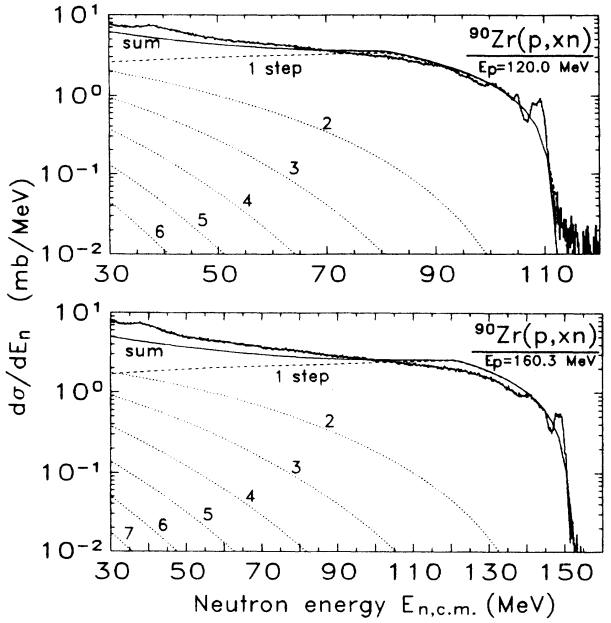

FIG. 8. Experimental angle integrated energy spectra for the reaction ^{90}Zr(p,n) in comparison to the standard hybrid model result (solid line). Also shown are the contributions of the first six (seven) steps.

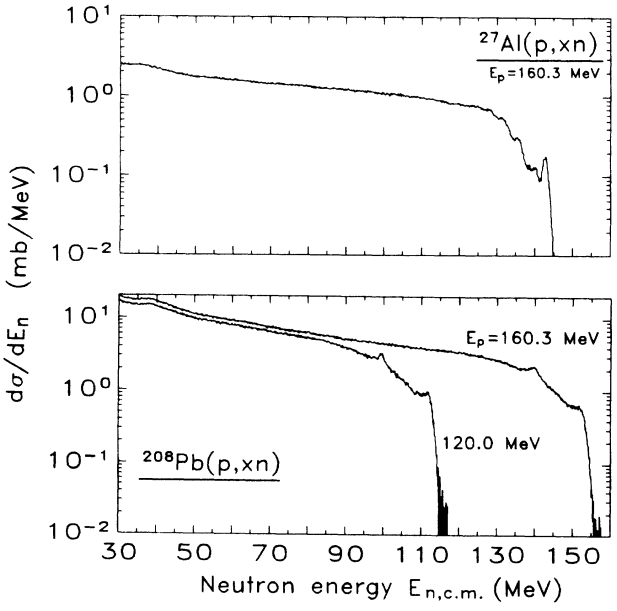

FIG. 9. Experimental angle integrated energy spectra for the reactions ^{27}Al and ^{208}Pb(p,n).

the first step contribution which comes from the $2p$-$1h$ configurations and amounts to more than 90% for $E_n \geq 0.5E_p$ (cf. Fig. 8) is too dominant in these semiclassical models. In passing we note that the shapes of the angle integrated spectra look very much the same for $p+^{27}$Al and ^{208}Pb (Fig. 9). Their absolute values follow a target mass dependence $d\sigma/dE_n \sim A^x$ with $x \approx 0.7$ for $E_p = 80$, 120, and 160 MeV, i.e., they exhibit a proportionality to the geometrical cross section ($x = 0.67$). All these features are indicative of a reaction mechanism that is composed of two[4] or a few more *direct* intranuclear nucleon-nucleon interactions.

IV. STATISTICAL MULTISTEP DIRECT EMISSION

The FKK multistep model[1] treats the nuclear reaction as a sequential process chained by a two-body interaction through states of increasing complexity. At each stage n, the theory differentiates between two classes of reaction amplitudes; an SMCE contribution connecting only particle bound states (which can be neglected here for $E_n \geq 0.5E_p$), and the SMDE contribution. The latter proceeds exclusively through states with at least one nucleon being unbound; its contribution to the double differential cross section can be calculated as[2]

$$\frac{d^2\sigma}{dU\,d\Omega} = \sum_{n=2}^{n_{\max}} \sum_{m=n-1}^{n+1} \int \frac{d\mathbf{k}_1}{(2\pi)^3} \cdots \int \frac{d\mathbf{k}_n}{(2\pi)^3} \left[\frac{dW_{m,n}(\mathbf{k}_f, \mathbf{k}_n)}{dU_f d\Omega_f} \right] \times \left[\frac{dW_{n,n-1}(\mathbf{k}_n, \mathbf{k}_{n-1})}{dU_n d\Omega_n} \right] \cdots \left[\frac{dW_{2,1}(\mathbf{k}_2, \mathbf{k}_1)}{dU_2 d\Omega_2} \right] \frac{d^2\sigma_{1i}(\mathbf{k}_1, \mathbf{k}_i)}{dU_1 d\Omega_1} \tag{3}$$

with the transition probability in the continuum region from the $(n-1)$th to the nth stage being, given by

$$\frac{d^2W_{n,n-1}}{dU_n d\Omega_n} = 2\pi^2 \rho_c(\mathbf{k}_n) \rho_n(U_n) |\langle \chi_n^- | V_{n,n-1} | \chi_{n-1}^+ \rangle|^2 . \tag{4}$$

The $\mathbf{k}_i$, $\mathbf{k}_\nu$, and $\mathbf{k}_f$ denote the momenta of the initial, νth intermediate, and final step nucleon, respectively; m labels the exit mode. The quantity $\rho_c(\mathbf{k})$ gives the density of states for particles of momentum $\mathbf{k}$ in the continuum, and U_j is the excitation remaining in the residual nucleus after step j. The SMDE cross section is thus expressed as a convolution of $n_{\max}$ incoherent single-step contributions with energy being conserved in each interaction. The matrix element describes the transition from the $(n-1)$th to the nth stage; it is evaluated in Born approximation with optical model (OM) generated distorted waves χ. $V_{n,n-1}$ is the matrix element connecting a nuclear state $n-1$ to a state n via the effective nucleon-nucleon interaction $V(r)$. The need for energy averaging of the distorted waves brings the matrix element in Eq. (4) in the DWBA form.[22] The energy averaging extends over many residual states in the energy interval dU_n such that interference terms are expected to cancel and the different orbital momenta L involved contribute incoherently. Accordingly, the entrance step is composed of an energy average over the density $\rho_2(U)$ of $1p$-$1h$ states in the nucleus after the first collision of the incident proton, the corresponding spin distribution function $R_2(L)$, and the DWBA cross section:

$$\frac{d^2\sigma_{1i}}{dU_1 d\Omega_1} = \sum_L (2L+1) R_2(L) \rho_2(U) \left\langle \frac{d\sigma_L^{(\mathrm{DW})}}{d\Omega} \right\rangle . \tag{5}$$

This single-step contribution is also added to the SMDE cross section of Eq. (3) in order to obtain the full direct cross section. All (partial) level densities ρ have been calculated with the equidistant Fermi gas model with Pauli corrections and a level density parameter $a = A/8.5$ MeV^{-1}; this implies the assumption of spectroscopic factors being equal to 1. All distorted wave functions were generated using the proton OM potential of Ref. 23, those for neutrons with the equivalent potential which was different only in the (opposite) sign of the asymmetry term. Further details are given in Refs. 2, 5, and 7.

For the residual interaction $V(r)$, a finite-range Yukawa potential with a range parameter $r_0 = 1$ fm has been chosen; its strength was initially set to the value $V_0 = 26 \pm 1$ MeV derived[3] for (p,n) reactions with $E_p \leq 25$ MeV. The (p,n) experiment[7] with $E_p = 80$ MeV projectiles on ^{90}Zr and ^{208}Pb led to angular and spectral distributions which were in conflict with $V_0 = 26$ MeV requiring a reduction to 20 ± 1 MeV. For further investigation we applied the SMDE model to the present (p,n) data keeping all parameters except V_0 fixed. It was then realized that convergence could no longer be obtained with $n_{\max} \leq 3$ as for $E_p \leq 80$ MeV, but required $n_{\max} = 6$ (5) for $E_p = 160$ (120) MeV. The contribution of the nth step is proportional to V_0^{2n}. Therefore, the absolute values of the calculated cross sections and (less pronounced) the slopes of the angular distributions are sufficiently sensitive to variations of V_0 to allow a fit to the experiment to within $\Delta V_0 = \pm 1$ MeV. This uncertainty also includes the systematic experimental uncertainties previously described.

Figure 10 shows some representative examples of the quality of fits obtained. The SMDE calculation is able to reproduce the angular distributions over more than 4 orders of magnitude. In particular, the agreement at backward angles where semiclassical PE models fail is remarkable. Fits of this quality could, however, only be obtained with a substantial reduction of V_0 to 16 ± 1 MeV for $E_p = 120$ MeV and further to 12.5 ± 1 MeV for $E_p = 160$ MeV.

This good agreement comes about through a delicate balance of first and higher order step contributions as a function of both, ejectile energy and angle. In Fig. 11,

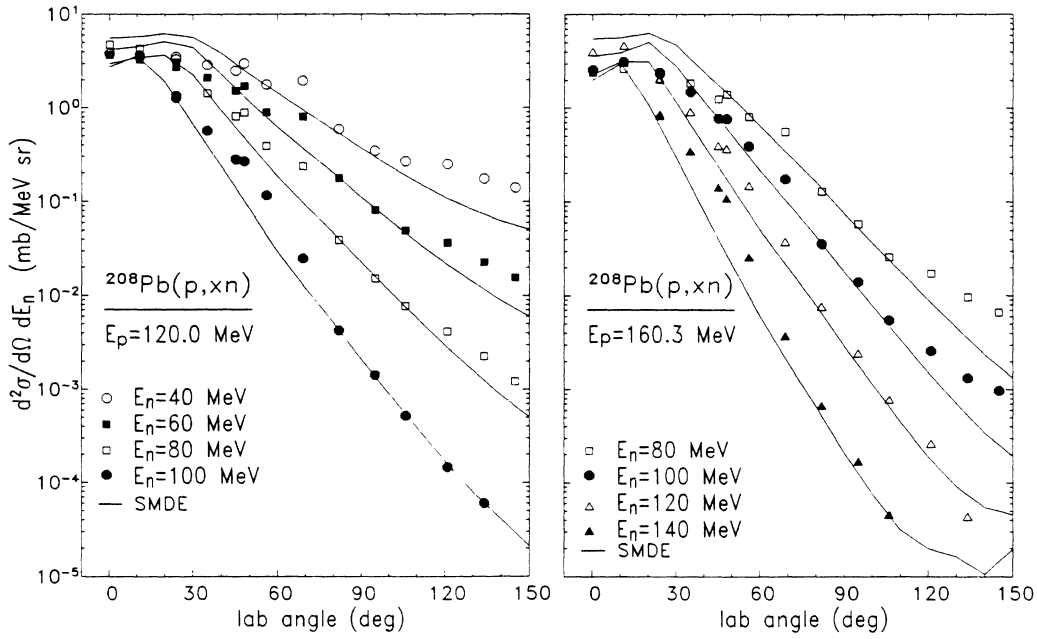

FIG. 10. Experimental angular distributions of neutrons of several c.m. energies for the reactions $p+^{208}$Pb in comparison to SMDE calculations with $V_0=16$ MeV (for $E_p=120$ MeV) and $V_0=12.5$ MeV (for $E_p=160$ MeV).

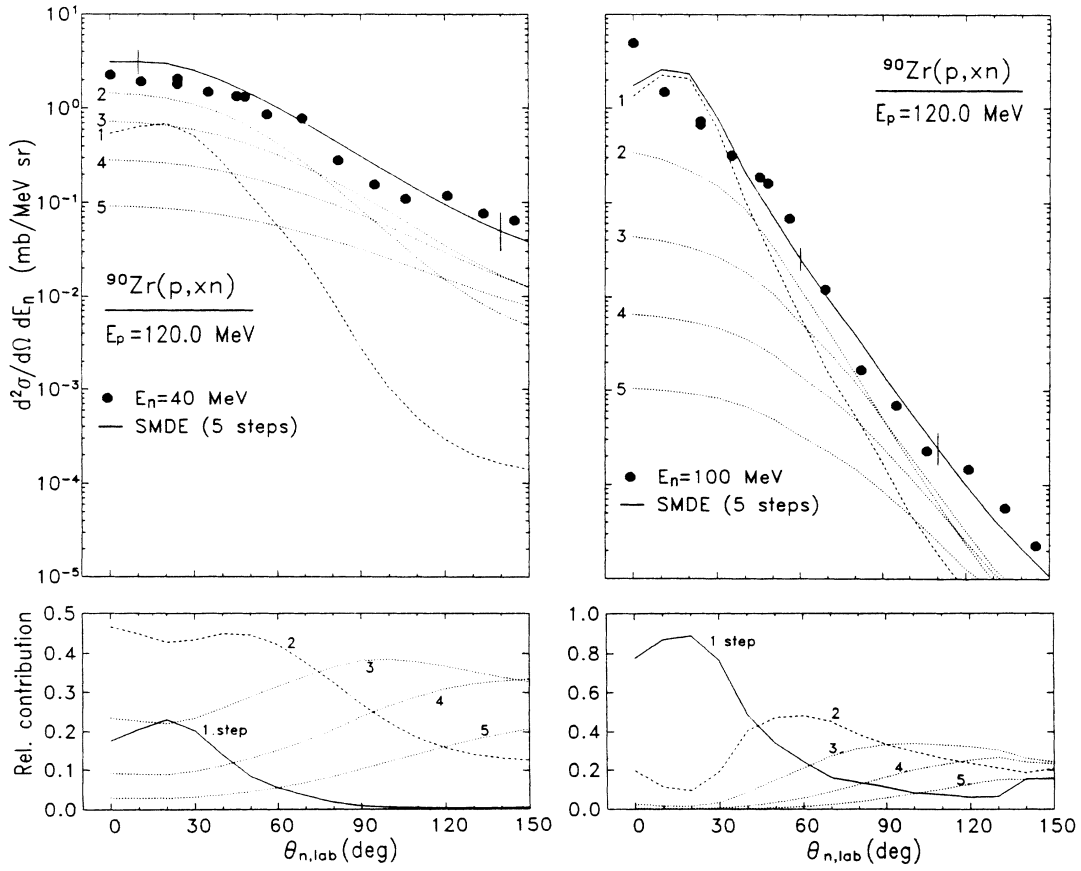

FIG. 11. Absolute (upper panels) and relative contributions of the leading five SMDE steps to the angular distribution of 40 and 100 MeV neutrons (c.m.) from ^{90}Zr(p,n) for $E_p=120$ MeV. The calculations were performed with $V_0=16$ MeV; the vertical bars indicate the variation for $\Delta V_0=\pm 1$ MeV.

the angular distributions for $p+^{90}$Zr with $E_p=120$ MeV at a low ($E_n=40$ MeV) and a high (100 MeV) neutron energy are shown separately in absolute and relative values for the first five steps. For forward angles the first step prevails for energies $E_n \geq 0.5E_p$, whereas for lower neutron energies the higher order contributions are important at all angles. In particular, the interval 45°–90°, where the angular distributions exhibit the maximum descent, is *not* dominated by the first step. For the higher projectile energy $E_p=160$ MeV, the situation is essentially the same (Fig. 12). For $\theta=10°$, the first two steps provide 80% or more of the total yield as predicted in Ref. 4; however, for $\theta=90°$, the contribution of the first step is—in agreement with the classical expectation—very low, and even the second step falls in relative yield behind the subsequent ones.

The lowest panel of Fig. 12 shows the relative SMDE contributions to the *angle integrated* spectrum. For $E_n \geq 120$ MeV, the first step provides at least 50% of the neutron yield, whereas for lower energies the second step is of comparable importance or even dominant. Again this weighting is essential for the agreement with experimental data. The semiclassical precompound models—the hybrid model[21] result is chosen for this comparison—overestimate the first step and accordingly end up with angular distributions which are too strongly peaked.

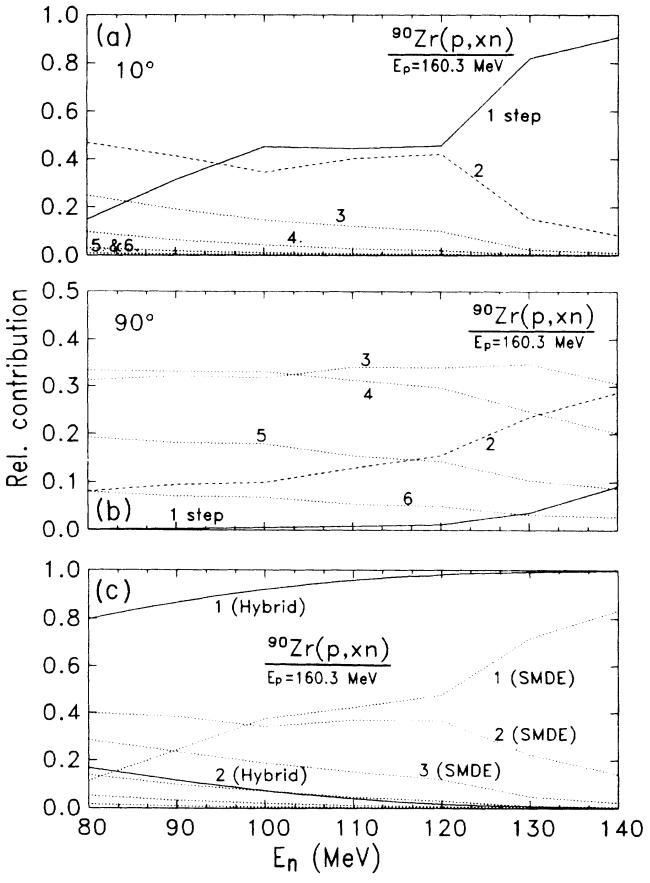

FIG. 12. (a) Relative contributions of the leading six SMDE steps to the neutron energy spectra from ^{90}Zr(p,n) for $E_p=160$ MeV and $\theta_{lab}=10°$. (b) Same as in (a) for $\theta_{lab}=90°$. (c) Same as in (a) for the angle integrated energy spectrum. Also shown are the first two hybrid model (Ref. 21) contributions.

The low weighting of the second generation contribution would be compensated to some fraction if the excitation distribution functions were evaluated rigorously,[24,25] but this effect is too small for high neutron energies to account for the discrepancy visible in Fig. 12(c). It rather rests in the different ways the depletion of higher order generations is taken care of. In the semiclassical (hybrid and exciton) model, the competition between emission and transition to the next higher stage is calculated explicitly with branching ratios. In the SMDE formalism, depletion is globally taken care of with the imaginary part of the OM potential; it is already present in the first step and decreases with nucleon energy, i.e., for higher order steps.

The moderate preponderance of the first step contribution visible in Fig. 12(c) is not in conflict with the results of Osterfeld *et al.*,[26] who analyzed ^{90}Zr(p,n) spectra, obtained for $E_p=200$ MeV in the forward ($\theta_{lab} \leq 18°$) region, with a large-basis random-phase approximation calculation. They reached the conclusion that for residual excitation $U \leq 70$ MeV, the spectra are the result of direct one-step processes, i.e., due to $1p$-$1h$ spin-isospin excitations of the target nucleus with $L=0$, 1, and 2, and contain only small contributions from more complicated multistep processes. Recent results on the ratio of non-spin-flip to spin-flip strength[27] and on (n,p) reactions[28] are in agreement with this interpretation.

The SMDE model is based on partial-state densities of the Fermi gas model and a spin-isospin independent interaction component V_0. Accordingly, it can only reflect the comparatively small "background" fraction due to single and multiple contributions resulting from V_0 for the extreme forward direction in the whole range of excitation energies over which the GT strength is distributed. This is the origin of the discrepancies observed at 0° for $E_n=100$ MeV (Fig. 11) and $E_n=140$ MeV (Fig. 7), and for $\theta=11°$ and $E_n=120$ MeV in Fig. 5.

However, beyond 20° the FKK model should be applicable, because in this range the GT strength is negligibly small; indeed the spectral shape calculated for $\theta=20°$ agrees with the experimental results (Fig. 3). The FKK theory predicts the angular distributions to flatten for $\theta \leq 30°$ (cf. Fig. 10). Therefore, the FKK calculation—or experimental spectra from $20° \leq \theta \leq 30°$—may provide an estimate of this "background" below the GT and IAS structure for $\theta < 20°$ with a normalization, e.g., for $E_n \approx 0.5E_p$.

Figure 13 summarizes the energy dependence of $V_0^2(E_p)$ deduced from the (p,n) data of this and of previous[3,7,29] work. The monotonic decrease of V_0 with increasing E_p qualitatively reflects the same trend in the central part of the spin-isospin independent effective nucleon-nucleon interaction.[9] The decrease is smoother than observed for the spectroscopic factors[30] derived from the DWBA analysis of ^{90}Zr(p,d) reactions populating low lying states. This is due to the fact that in our calculations we apply a fixed value V_0 for all steps; how-

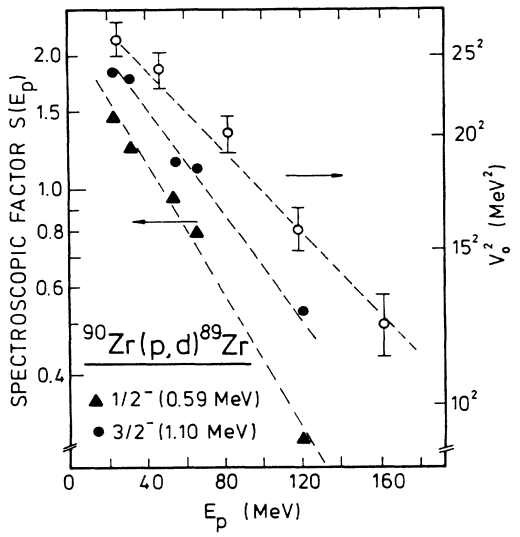

FIG. 13. SMDE best fit values V_0^2 of this work (open circles) and spectroscopic factors for the ^{90}Zr(p,d) transition to the excited state indicated (Ref. 30). The dashed lines are drawn to guide the eye.

ever, from the second step on, scattering takes place with progressively smaller kinetic energies which in turn would require correspondingly larger values of V_0. The values of V_0 deduced in this way therefore represent averages over all steps [cf. Fig. 12(c)] and energies involved in the nucleon-nucleon interaction cascade. In contrast, the spectroscopic factors may be dependent on the nuclear wave functions; they probe only the single-step direct interaction. This is also evidenced by the agreement of their dependence on E_p with that of the volume integrals for the respective proton OM potentials.[30]

V. SUMMARY

We have measured the inclusive double differential cross sections for the (p,n) reactions on ^{27}Al, ^{90}Zr, and ^{208}Pb for projectile energies of 120 and 160 MeV in the spectral continuum $E_n \geq 30$ MeV. In the experiment, emphasis was put on neutron TOF spectroscopy over a wide angular ($\theta = 0°-145°$) and intensity ($d^2\sigma/d\Omega\, d\epsilon \geq 10^{-4}$ mb/sr MeV) range with careful consideration of background problems. The data obtained are well reproduced by the phenomenological parametrization of Kalbach.[17]

The theoretical analysis concentrates on the multistep direct emission process. We find that the statistical multistep direct emission as described in the quantum statistical model of Feshbach *et al.*,[1] provides the link between the single-step DWBA calculations as one picture and the composite system with only bound nucleons as the other extreme. The number of steps n_{max} necessary to reproduce double differential (p,n) cross sections for $E_n \geq 0.5E_p$ quantitatively increases with projectile energy. The failure of semiclassical preequilibrium models in reproducing angular distributions is traced back to insufficient contributions from stages $n \geq 2$. The energy dependence resulting for the only free parameter, the strength $V_0(E_p)$ of the (spin and isospin independent) effective nucleon-nucleon interaction, is found to be consistent with calculations of spectroscopic factors and of effective nucleon-nucleon interactions.

ACKNOWLEDGMENTS

The authors acknowledge the hospitality and cooperation of the Indiana University Cyclotron Facility (IUCF) staff for making this work possible. This work was supported in part by the BMFT (Vorhaben 06-HH-142), the INFN, Sezione di Milano and by the Department of Energy under Contract No. W-7405-Eng-48.

[1] H. Feshbach, A. Kerman, and S. Koonin, Ann. Phys. (N.Y.) **125**, 429 (1980).
[2] R. Bonetti, M. De Camnasio, L. Colli-Milazzo, and P. E. Hodgson, Phys. Rev. C **24**, 71 (1981).
[3] E. Mordhorst, M. Trabandt, A. Kaminsky, H. Krause, W. Scobel, R. Bonetti, and F. Crespi, Phys. Rev. C **34**, 103 (1986), and references therein.
[4] H. C. Chiang and J. Hüfner, Nucl. Phys. **A349**, 466 (1980).
[5] R. Bonetti and R. Colombo, Phys. Rev. C **28**, 980 (1983).
[6] S. M. Austin, in *The (p,n) Reaction and the Nucleon-Nucleon Force*, edited by C. D. Goodman *et al.* (Plenum, New York, 1980).
[7] M. Trabandt, W. Scobel, M. Blann, B. A. Pohl, R. C. Byrd, C. C. Foster, S. M. Grimes, and R. Bonetti, Phys. Rev. C **39**, 452 (1989).
[8] W. G. Love and M. A. Franey, Phys. Rev. C **24**, 1073 (1981).
[9] M. A. Franey and W. G. Love, Phys. Rev. C **31**, 488 (1985).
[10] C. D. Goodman, C. C. Foster, M. B. Greenfield, C. A. Goulding, D. A. Lind, and J. Rapaport, IEEE Trans. Nucl. Sci. **26**, 2248 (1979).
[11] D. L. Friesel, R. E. Pollock, T. Ellison, and W. P. Jones, Nucl. Instrum. Methods B **10-11**, 864 (1985).
[12] R. A. Cecil, B. D. Anderson, and R. Madey, Nucl. Instrum. Methods **161**, 439 (1979).
[13] J. W. Watson, R. Pourang, R. Abegg, W. P. Alford, A. Celler, S. El-Kateb, D. Frekers, O. Häusser, R. Helmer, R. Henderson, K. Hicks, K. P. Jackson, R. G. Jeppesen, C. A. Miller, M. Vetterli, S. Yen, and C. D. Zafiratos, Phys. Rev. C **40**, 22 (1989).
[14] R. C. Byrd and W. C. Sailor, Nucl. Instrum. Methods A **274**, 494 (1989).
[15] D. E. Bainum, J. Rapaport, C. D. Goodman, D. J. Horen, C. C. Foster, and M. B. Greenfield, Phys. Rev. Lett. **44**, 1751 (1980).
[16] T. N. Taddeucci, C. D. Goodman, R. C. Byrd, I. J. Van Heerden, T. A. Carey, D. J. Horen, J. S. Larsen, C. Gaarde, and E. Sugarbaker, Phys. Rev. C **33**, 746 (1986).
[17] C. Kalbach, Phys. Rev. C **37**, 2350 (1988).
[18] C. Kalbach and F. M. Mann, Phys. Rev. C **23**, 112 (1981).
[19] M. Blann, W. Scobel, and E. Plechaty, Phys. Rev. C **30**, 1493 (1984).
[20] H. Gruppelaar, P. Nagel, and P. E. Hodgson, Riv. Nuovo

Cimento **9**, 1 (1986).
[21]H. Blann and H. K. Vonach, Phys. Rev. C **28**, 1475 (1983).
[22]H. Feshbach, Ann. Phys. **159**, 150 (1985).
[23]P. Schwandt, H. O. Meyer, W. W. Jacobs, A. D. Bacher, S. E. Vigdor, M. D. Kaitchuk, and R. T. Donoghue, Phys. Rev. C **26**, 55 (1982).
[24]J. Bisplinghoff, Phys. Rev. C **33**, 1569 (1986).
[25]M. Blann and J. Bisplinghoff, Z. Phys. A **326**, 429 (1987).
[26]F. Osterfeld, D. Cha, and J. Speth, Phys. Rev. C **31**, 372 (1985).
[27]H. Sakai, N. Matsuoka, T. Saito, A. Shimizu, M. Tosaki, M. Ieiri, K. Imai, A. Sakaguchi, and T. Motobayashi, Phys. Rev. C **35**, 1280 (1987).
[28]F. P. Brady, T. D. Ford, J. L. Romero, J. R. Drummond, E. L. Hjort, N. S. P. King, B. McEachern, D. S. Sorensen, Zin Aung, A. Klein, W. G. Love, and J. K. Wambach, Phys. Rev. C **40**, R475 (1989).
[29]M. Blann, R. R. Doering, A. Galonsky, D. M. Patterson, and F. E. Serr, Nucl. Phys. **A257**, 15 (1976).
[30]S. Kosugi and T. Kosugi, Phys. Lett. **127B**, 389 (1983).